Available online at www.sciencedirect.com

jmr&t Journal of Materials Research and Technology

journal homepage: www.elsevier.com/locate/jmrt

Original Article

The evolution of precipitates in an Al–Zn–Mg alloy

E. Thronsen [a,*,1], S. Shah [b], C. Hatzoglou [b], C.D. Marioara [c], S. Wenner [a,c], S.J. Andersen [c], B. Holmedal [b], R. Holmestad [a]

[a] Department of Physics, Norwegian University of Science and Technology (NTNU), N-7491, Trondheim, Norway
[b] Department of Materials Science and Engineering, NTNU, N-7491, Trondheim, Norway
[c] Materials and Nanotechnology, SINTEF Industry, N-7465, Trondheim, Norway

ARTICLE INFO

Article history:
Received 17 January 2023
Accepted 19 February 2023
Available online 1 March 2023

Keywords:
Aluminum alloys
Transmission Electron Microscopy (TEM)
Precipitates
Atom Probe Tomography (APT)
GP-zones

ABSTRACT

The precipitation sequence in Al–Zn–Mg alloys has been subject to many revisions over the years as more structural details of the early-stage Guinier-Preston (GP) zones and precipitates have been uncovered. To further investigate this, a 7003 aluminium alloy naturally aged for one year was subjected to artificial ageing at 140 °C to investigate the evolution of early-stage precipitates. Scanning transmission electron microscopy was coupled with atom probe tomography and hardness measurements to characterise the precipitate structure and chemistry of the alloy at different stages in the heat treatment. The naturally aged condition contained a dense population of GPI zones, co-existing with a smaller distribution of η' precipitates. After artificial ageing for 10 min, the hardness decreased from 121 HV to 88 HV. The number densities of clusters were similar in the two conditions, while the average size of the clusters had increased during the first 10 min of artificial ageing. The average Zn/Mg ratio of the clusters decreased from 2.0 to 1.7 and the clusters no longer exhibited the GPI zone atomic structure, indicating that the GPI zones had dissolved. Concurrently, the fraction of precipitates having η' structure increased from 2% to 18%. During further ageing, the hardness increased again, reaching a peak after 5 h. In this condition, η' was the dominant phase, co-existing with η_1, η_2 and T′ phases. Atomically resolved scanning transmission electron microscopy images in addition to precession electron diffraction patterns of the disputed T′ phase are presented and compared to literature.

1. Introduction

The Al–Zn–Mg alloy system comprises a set of medium to high strength age-hardenable Al alloys [1]. They gain their strength by the formation of metastable, semi-coherent, nano-sized precipitates during artificial ageing (AA). The precipitates are effective in impeding dislocation motion, hence a large number density of precipitates is normally associated

* Corresponding author.
E-mail address: Elisabeth.thronsen@sintef.no (E. Thronsen).
[1] Permanent address: Materials and Nanotechnology, SINTEF Industry, N-7465, Trondheim, Norway.

https://doi.org/10.1016/j.jmrt.2023.02.144

with high strength. The precipitation is usually given as a sequence [2–4]:

$$\mathrm{SSSS} \rightarrow \mathrm{solute\,clusters} \rightarrow \mathrm{GPI/GPII\,zones} \rightarrow \eta' \rightarrow \eta_{1-14} \rightarrow \eta(\mathrm{MgZn_2}), \quad (1)$$

describing the evolution of precipitates following the solution heat treatment (SHT), conducted at temperatures above the solvus line of the system. The SHT is usually followed by a quench to room temperature (RT), forming a state of supersaturated solid solution (SSSS). This state is associated with a higher density of vacancies and solutes in solid solution compared to the equilibrium condition, increasing with the quench rate. The SSSS is unstable and if kept at RT, solute clusters form, which is accompanied by a gradual increase in hardness. This phenomenon is known as natural ageing (NA). The clusters are solute orderings constituting a supercell in the Al matrix. Depending on the structure of the cluster, the misfit with Al may be non-isotropic, resulting in plate- or disk shaped clusters. The initial solute clusters in Al alloys system are often considered disordered [5]. When order is detected, they are referred to as a Guinier-Preston (GP) zones [6,7]. Maximum hardness is achieved by AA at elevated temperatures, due to coherence strain from a high density of solute-rich, plate-like η' precipitates on $\{111\}_{Al}$ planes. Upon further ageing, the hardness decreases due to coarsening and transformation towards the equilibrium η-$MgZn_2$ phase. There are fourteen reported orientation relationships of η-phases with the Al matrix [8–14]. The ones relevant for the present work are listed in Table 1.

Two types of GP zones, the spherical GPI and the disk-like GPII zones, have been reported in Al–Zn–Mg alloys [2,17]. The crystal structure of the GPI zones was recently solved by Lervik et al. [18], who found that their structure could be described by solutes arranging in the Al matrix in molecular cluster units of high symmetry termed truncated cube octahedron (TCO)s. The TCO may be understood as an Al cube unit with 8 Mg at the corners, 6 Zn on the faces, centered around a possible interstitial of Al, Zn or Mg. The immediate shell of 24 atoms around the cube unit constitutes the TCO, exhibiting a high Zn concentration. Several such units connect along specific Al fcc directions to form lager zones [18,19]. While the structure of the GPII zones is not yet resolved, they are reported to be plates on $\{111\}_{Al}$ planes, comprising a few atomic layers. They are regarded as precursors of the η' precipitates [17,20].

In addition to exhibiting different morphologies and crystal structures, the GPI and GPII zones are observed after different ageing treatments. The GPI zones are reported to form from RT and up to the upper limit for GPI formation T_h, which depends on the solute concentration of the alloy [2,3]. In general, the dissolution temperature for the GPI zones, T^{GPI}_{diss} does not coincide with T_h. A thorough review of T_h and T^{GPI}_{diss} for different Al–Zn–Mg alloys can be found in the review article by Löffler et al. [2]. The GPII zones have been observed after quenching from SHT temperatures above 450 °C and at AA temperatures above 70 °C [17].

For optimal strength, the Al–Zn–Mg alloys usually undergo a two-step ageing treatment [21]. The first step is typically executed at temperatures below T_h, e.g. 100 °C, the second step above T^{GPI}_{diss}, e.g. 150 °C [3,17]. Early works have shown that ageing at RT prior to AA benefits the nucleation of the main hardening phase, η' [11,22–24]. Initially, a transient drop in the hardness is observed during the second step of the ageing. This is known as *the reversion* and is attributed to the dissolution of the GP zones [2]. Two types of reversion have been observed: *Partial* and *complete reversion*. During partial reversion, the strength does not recover to the as-quenched level. Some authors claim that this is caused by a fraction of GP zones acting as nuclei for the hardening η' phase [25]. Other authors reason that during the first step of ageing, two types of clusters form, namely the GP zones and vacancy-rich clusters (VRC) [2]. The VRC was introduced to explain why indirect quenching, i.e. quenching to RT before AA, was more beneficial for the nucleation of η' compared to direct quenching to the ageing temperature [26]. During complete reversion, the GP zones fully dissolve prior to the nucleation of η'. It is possible that the η' nucleates on the small clusters produced in the final stages of dissolution of the zones, explaining the effectiveness of two-step ageing [2]. The stability of the GP zones against reversion heat treatments increases with increasing GP zone sizes, which is dependent on the alloy composition and heat treatment [2].

The most frequent precipitate phases observed after AA are η', η_1, η_2, which are found to be homogeneously distributed [4,12,16]. The η_4 is primarily associated with defects and hence heterogeneously distributed [4,12,16]. All the orientation relationships of η, η_1-η_{14}, have identical bulk structures, however they connect with the Al matrix in different ways, thus having different interfaces. The η' precipitate and most of the orientation relationships between η and Al have been known and studied for decades [8–12]. Their bulk and interface structures were solved by atomically resolved high-angle annular dark field (HAADF)-scanning transmission electron microscopy (STEM), where the atom columns are more directly interpretable as compared to high-resolution TEM (HRTEM). Marioara et al. [15] presented the first atomically resolved HAADF-STEM images of η' and η_2 precipitates along the $\langle 211\rangle_{Al}$ direction and labeled them 'Type 1' and 'Type 2', respectively. The atomic models for η' and η_2 presented in Ref. [15] are shown in Fig. 1a and b, respectively. These precipitates have the same orientation relationship and habit planes. η' can be described as consisting of one

Table 1 – Habit planes, morphologies and orientation relationships between η precipitates and the Al matrix reported in the present study.

	Orientation relationship		Habit plane	Morphology	Reference
η' (Type 1)	$[100]_\eta//[112]_{Al}$	$[120]_\eta//[\bar{1}10]_{Al}$	$(001)_\eta//(111)_{Al}$	Plate	[4,8,15,16]
η_2 (Type 2)	$[100]_\eta//[112]_{Al}$	$[120]_\eta//[\bar{1}10]_{Al}$	$(001)_\eta//(111)_{Al}$	Plate	[9,13,15]
η_1	$[100]_\eta//[\bar{1}10]_{Al}$	$[120]_\eta//[001]_{Al}$	$(001)_\eta//(\bar{1}10)_{Al}$	Plate	[4,9,13,16]

rhomobohedral (R) and one orthorombic unit (O) when viewed along $\langle 211\rangle_{Al}$, thus having a fixed width (i.e. plate thickness) of $6d^{Al}_{111}$ [15,28–30]. The O and R layers are visualised in Fig. 1a η_2 on the other hand, can be described as layers of R units on $\{111\}_{Al}$ planes, the units can be parallel (R) and/or mirrored (R^{-1}) when viewed along $\langle 211\rangle_{Al}$ [13,15,28,30,31], as visualised in Fig. 1b. The η-$MgZn_2$ is essentially a zig-zag stacking of such layers ($RR^{-1}RR^{-1}$..) and is isostructural with η_2, if the solute-enriched $\{111\}_{Al}$ interface planes are neglected [15]. Bendo et al. [16] investigated the η_1 precipitate and found that it consisted of a pairwise stacking of R and R^{-1} layers when viewed along $[010]_{\eta 1}//[110]_{Al}$.

Many authors report that the η' transforms into η_2 during artificial ageing [12,13,20,32]:

$$\eta' \rightarrow \eta_2 \rightarrow \eta. \quad (2)$$

Other authors have identified an additional η precursor phase and its GP zone, η_p and GP-η_p, respectively, yielding the following precipitation sequence [33–36]:

$$GP - \eta_p \rightarrow \eta_p \rightarrow \eta. \quad (3)$$

By inspection of HAADF-STEM images however, it is evident that the precipitate structures GP-η_p and η_p exhibit the same atomic structure as η' and η_2, respectively. This misconception may be explained by the varying sizes of both precipitates affecting the intensities in HAADF-STEM and HRTEM images, since the size of the precipitate and its position in the Al matrix strongly affect the image contrast. Precipitates embedded in Al along the viewing direction yield a contrast different from precipitates occupying the whole thickness of the TEM sample. This is often not accounted for in image simulations, leading to misinterpretation of the simulated images. In general, precipitates with habit plane $(001)_{\eta}//(111)_{Al}$ and the following orientation relationship: $[100]_{\eta}//[112]_{Al}$ and $[120]_{\eta}//[110]_{Al}$ can be categorised based on the following criteria:

- η': 7 atomic layers with a width of $6d^{Al}_{111}$. One R and one O layer.
- η_2: 11 atomic layers or more with a width of at least $9d^{Al}_{111}$. R and R^{-1} layers.

The η' and η_{1-2} precipitates can have imperfect stacking [4,15,16,29,31,37]. Some precipitates do not follow the criteria given above. These structures consist of multiple R-, R^{-1} and O layers, referred to as η' and η'_p in Refs. [36,38] and Ref. [35], respectively. The two precipitation sequences in Eq. (2) and Eq. (3) are identical if applying the categorising criteria above. In this work we will adapt the naming convention used by Chung et al. [13].

In addition to η and its precursors, the equilibrium phase T-$Mg_{32}(AlZn)_{49}$ and its precursors have also been observed in Al–Zn–Mg alloys with moderate to high Mg/Zn ratio [2,39,40]. The phase has a large, cubic unit cell and belongs to space group Im^{-3} with lattice parameter $a_0 = 14.16$ A [39,41]. The cell has 256 atoms. The T phase is preceded by the metastable, semi-coherent T′ phase [42–46]. The orientation relationship between the T/T′ phases and the Al matrix is often reported as $(100)_T//(112)_{Al}$ and $(001)_T//(110)_{Al}$ [2]. Other orientation relationships have been reported, e.g. the one reported by Guo et al. [47] $(100)_T//(100)_{Al}$ and $(001)_T//(011)_{Al}$. Early studies indicate that the T phase and its precursor had approximately the same composition [42], although more recent atom probe tomography (APT) and energy-dispersive X-ray spectroscopy (EDS) studies report that the T′ phase is more Mg-rich compared to the stable T phase [45,48]. Recently, Zou et al. [49–51] have reported the co-existence of Zn-rich T′ and η' precipitates in Al–Zn–Mg alloys.

In the present study, we use transmission electron microscopy (TEM) in conjunction with APT studies and hardness measurements to investigate the evolution of the precipitates in a commercial 7003 alloy for different AA times after one year storage at RT. Atomically resolved HAADF-STEM is employed to investigate the atomic structure of clusters and precipitates, while scanning precession electron diffraction (SPED) is used to obtain diffraction patterns from individual precipitates. The APT technique is complementary to TEM and gives reliable statistics of clusters and precipitation in terms of size and number densities, as well as giving information about the chemistry of both the particles and the Al matrix. The goal is to improve the understanding of the transformation from GPI zones to η' and other η variants and to investigate the reversion phenomena by the means of modern characterisation tools. To the best of our knowledge, we also present the first time HAADF-STEM images of the T′ phase.

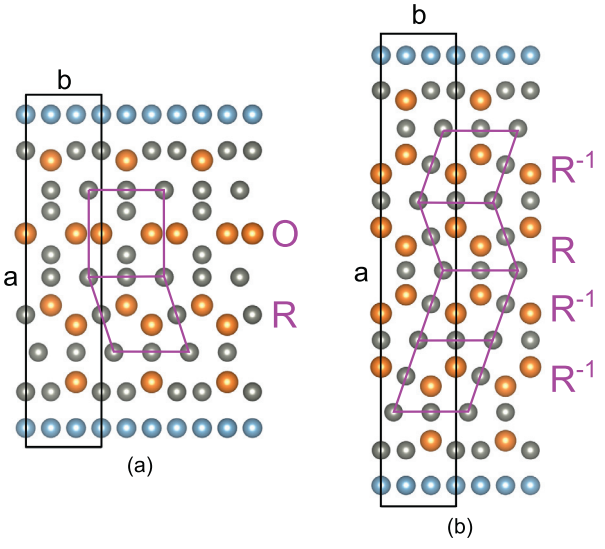

Fig. 1 – (a): The projected atomic structure of η' along $\langle 211\rangle_{Al}$, indicating its characteristic O and R layers. (b): The projected atomic structure of η_2 along $\langle 211\rangle_{Al}$, indicating its characteristic R and R^{-1} layers. The atomic structures were visualised using Vesta [27].

2. Material and methods

2.1. Material

The investigated material was 6 mm thick, extruded plates of a commercial 7003 Al alloy, which were supplied by Benteler Automotive. The composition of the alloy is shown in Table 2. The samples underwent SHT at 480 °C for 30 min in a salt bath. Immediately after the SHT the samples were water quenched followed by a NA treatment for 1 year. The samples subsequently underwent AA at 140 °C for different times in an oil bath.

2.2. Hardness measurements

Samples were cut into 3 × 3 cm^2 for Vickers hardness measurements. They were grounded and polished. Hardness was measured using a 1000 gf Vickers indenter. The hardness in a given condition is the average of four independent indents.

2.3. Atom probe tomography

APT samples for all the three conditions were prepared by following a standard two-step electropolishing process [52]. A minor contamination of Cu on the surface of the tip was detected, similar to the observations in Refs. [53,54]. This is believed to be an artefact due to copper deposition after electropolishing and is also observed in electropolished TEM samples [55]. Thus, the Cu-enriched volume close to the surface was excluded in the analysis.

The APT experiments were performed using a Local Electrode Atom Probe (LEAP) 5000XS by Cameca instruments Inc. It has a detection efficiency of 80% and is a straight flight path instrument. The base temperature was set to 30 K and the laser pulse mode was used with an equivalent pulse fraction of 20% calibrated to around 70–100 pJ depending on the sample geometry. A detection rate of 0.5% and a pulse frequency of 250 kHz were used for all of the experiments. Datasets containing 20–35 million ions were collected. The reconstructions and the post processing analyses were carried out using the Integrated Visualisation and Analysis Software (IVAS) by Cameca Instruments Inc. The Norwegian Atom Probe App (NAPA) software [56] was used for cluster identification, composition measurements and best fit ellipsoid (BFE) [57] for the size estimations. Reconstructions were done using the structural information according to Gault et al. [58].

The iso-position method (IPM) enabled identification of the particles in all the APT datasets. This method has been developed at the Groupe de Physique des Materiaux (University of Rouen, France) and is based on the chemical concentration (i.e. Mg + Zn) and atomic distance criteria. A more detailed description can be found in Refs. [59,60]. All the identified particles exhibit an excess atomic density compared to the surrounding matrix (up to 5 times), suggesting the presence of local magnification effects [61,62]. The particle morphological variation observed by Shah et al. [63] on the same alloy confirms this hypothesis. This well-known APT artefact strongly modifies the apparent reconstructed particle morphology [64,65]. For each particle in the aged condition, a BFE was estimated to extract the principal dimensions of a particle (L_3, L_2 and L_1 where $L_3 \leq L_2 \leq L_1$) [57]. However, it was not possible in the present study to distinguish particles as a function of their morphology (rod (η), plate (η), or spheroidal (GPI or T')) as in e.g. Ref. [66]. The particle size is estimated as $L_3/2$. For a rod-shaped particle, the size corresponds to the half-length, while for a spheroidal or plate-like particle, the size correspond to the radius. It should be noted that these dimensions may be influenced by the local magnification effect [57,61,65], which depends on the particle morphology and orientation.

The errors in size were calculated based on standard deviation between the particles, while the error in the number density was calculated by dividing the number density with the square root of the total number of particles. Particles located at the edges of the datasets are counted as half a particle upon calculating the number density and they are identified using the method by Jenkins et al. [67].

2.4. Transmission electron microscopy

Specimens for TEM were prepared by grinding down bulk samples to ≈100 μm thickness, punching out disks of 3 mm diameter and subsequently electropolishing in a Struers TenuPol-5 machine using an electrolyte mixture consisting of 1/3 HNO_3 and 2/3 CH_3OH. The liquid was kept at −25 °C ± 5 °C and the applied voltage was 20 V.

An image and probe corrected JEOL JEM-ARM200CF microscope operated at 200 kV was used to acquire the HAADF-STEM images. For the acquisition, the convergence semi-angle was 27 mrad and the inner and outer collection semi-angles were 67 mrad and 155 mrad, respectively. The probe current was about 60 pA, which gives a good signal and sufficient spatial resolution. Some of the HAADF-STEM images were filtered by performing a fast Fourier transform (FFT) and then applying a low-pass mask on the FFT of approximately 6.7 nm^{-1} before performing an inverse FFT. This reduces the high-frequency noise in the images, enhancing the contrast of the clusters and precipitates in the subsequent inverse FFT images. Smart Align (HREM Research Inc.) was used in the acquisition of some of the images. This involves acquiring a stack of successive low-dose images and afterwards aligning them to correct both rigid and non-rigid scan distortions [68].

A JEOL 2100 F microscope operated at 200 kV was used for the SPED experiments. During SPED acquisition, the microscope was operated in the nanobeam diffraction mode, using a convergence angle of 1 mrad. The precession angle and frequency were 0.5° (= 8.7 mrad) and 100 Hz, respectively. The scan step size was set to 0.93 nm and the scans were 100 × 100 pixels. The probe size was about 1 nm. The double-rocking probe was aligned according to the approach described by Barnard et al. [69]. The SPED was performed using the

Table 2 – The composition of the investigated alloy.

	Zn	Mg	Fe	Si	Zr	Ti
at.%	2.43	0.84	0.11	0.09	0.05	0.01
wt.%	5.68	0.73	0.22	0.09	0.15	0.02

NanoMEGAS DigiSTAR control software. The 4D SPED datasets were recorded using a Medipix3 MerlinEM camera from Quantum detectors with a 256 × 256 Si chip [70]. The diffraction patterns were recorded in the 12 bit mode, using an exposure time of 40–60 ms per pixel, ensuring sufficient counts for identifying the patterns. To enhance the signal/noise ratio, each PED pattern shown is the average of multiple PED patterns from the same precipitate. The SPED data was analysed using the open source python library pyxem [71] and a simplified version of the approach described in Ref. [19].

3. Results

3.1. *Hardness evolution*

The hardness as a function of AA time is shown in Fig. 2. The first measurement point (NA) corresponds to the hardness after one year of NA and reads 121 HV. After 10 min of the AA treatment, the hardness drops to 88 HV, indicated by 'Dip' in Fig. 2. This is significantly higher than the as-quenched hardness, which for this alloy and this SHT is 47 HV. The hardness subsequently increases, until it reaches a peak age hardness of 122 HV after 5 h, labeled 'Peak' in Fig. 2. The yellow points indicate conditions investigated by APT and TEM and will in the following be termed 'NA', 'Dip' and 'Peak' conditions corresponding to 1 year NA, 1 year NA + 10 min AA and 1 year NA + 5 h AA, respectively.

3.2. *Particle statistics by APT*

3D-elemental maps of the APT datasets from the NA, dip and peak conditions are shown in Fig. 3a. Based on the size of the observed particles, they can be classified as either clusters or precipitates. The radial distribution functions of Mg and Zn for the three conditions are shown in Fig. 3b. The NA and dip conditions exhibit homogeneous distributions of small particles enriched in both Zn and Mg. In the peak condition, the top of the APT map volume contains a dense and homogeneous precipitate distribution. The lower part is less dense, probably due to the presence of three larger precipitates in this region, which may indicate that there is a defect such as a grain boundary in the volume.

Number densities and average particle sizes were quantified for all three conditions and the results are shown in Table 3. For the NA and dip conditions, the whole APT volume was used for the quantification, while for the peak condition, only particles above the dashed line in Fig. 3a were included, due to the less homogeneous microstructure below the dashed line. The TEM investigations probed volumes much larger than the APT investigations and found a homogeneous microstructure, justifying the neglection of particles below the dashed line.

From Table 3 it can be seen that the number densities of particles in the NA and dip condition are similar. The size however increases slightly between NA and the dip condition. The particle size distributions for all three conditions are given in Fig. 4 showing that the peak of the size distribution is shifted to larger sizes in the dip condition. At the peak condition, the number density significantly decreases, correlated with a modest increase in the average particle size as compared to the dip condition, c. f. Table 3. As seen in Fig. 4, the particle size distribution in the peak condition has a larger spread and does not exhibit a clear peak.

The estimated Mg and Zn and Mg + Zn compositions of the bulk, matrix and particles along with the Zn/Mg ratio of the particles are shown in Table 4 for all three conditions. The Zn/Mg ratio of the particles in the NA condition is 2.0 and decreases to about 1.7 in the dip condition. It is noted that the solute content of the matrix slightly decreases between the NA and dip condition, while the solute content of the particles is

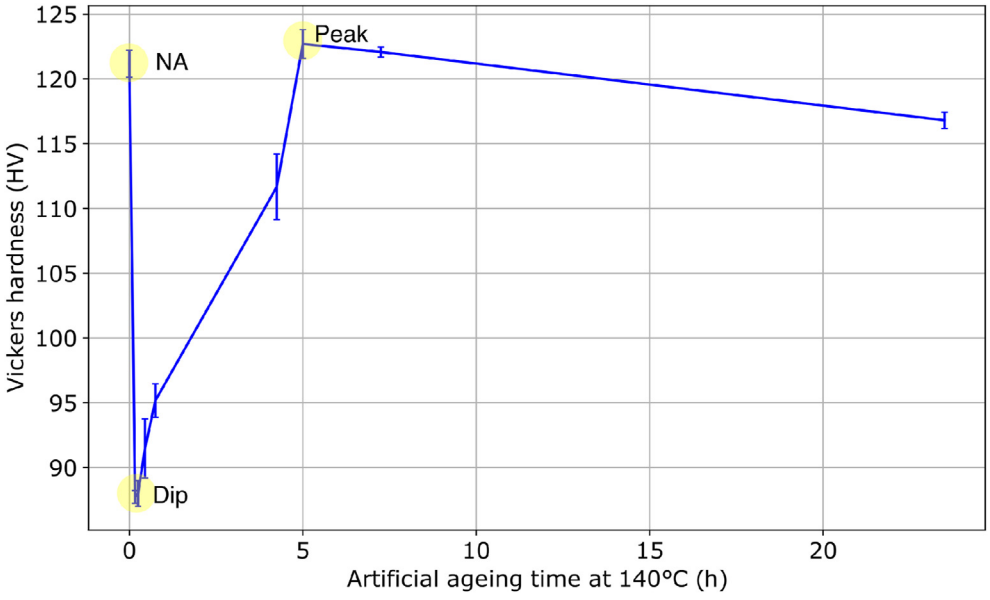

Fig. 2 – The hardness as a function of artificial ageing time at 140 °C. The first measurement shows the hardness after 1 year NA. The yellow points indicate conditions investigated by TEM and APT.

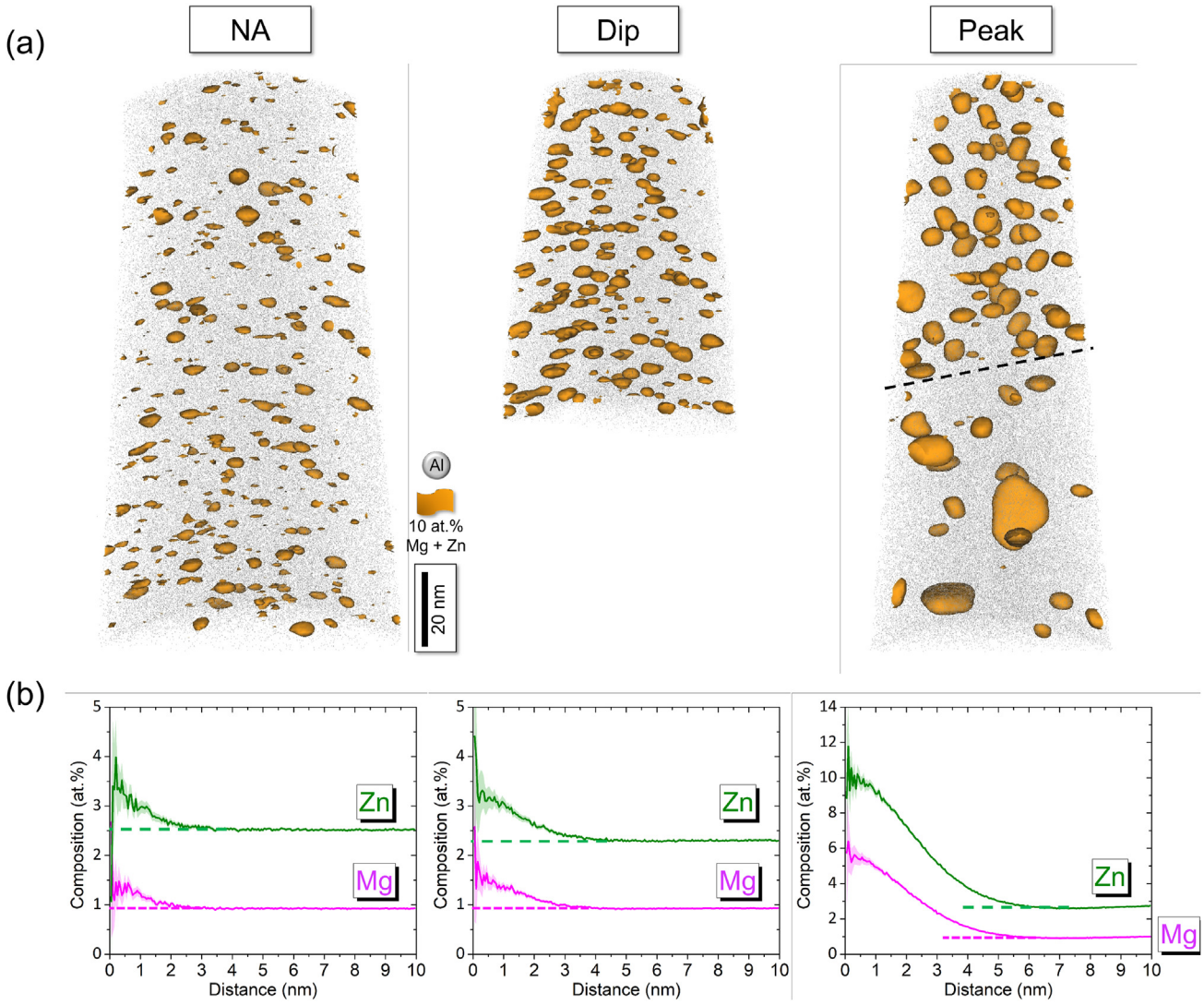

Fig. 3 – (a): 3D atom probe reconstructions showing particles enriched in Mg and Zn, with iso-composition surfaces at 10 at.% of Mg + Zn, embedded in Al matrix (in gray). (b): radial distribution function of Mg and Zn centered to Mg atoms for NA, dip and peak conditions.

Table 3 – Number density and average size for NA, dip and peak conditions. For the peak condition, only particles above the line in Fig. 3a where taken into account.

	NA	Dip	Peak
Number density ($10^{23}/m^3$)	8.89 ± 0.38	8.95 ± 0.65	5.05 ± 0.45
Size (nm)	1.64 ± 0.69	2.05 ± 0.83	2.24 ± 1.44

similar. The compositions were estimated using two different approaches, the matrix compositions were estimated by using the distribution of isolated atoms for the determination of the matrix composition (DIAM) method [72], while the particle compositions were estimated using the IPM [59]. The fact that the estimations of solutes in solid solution decreases in the matrix while staying constant in the particles implies that the precision of the estimation methods or the mass resolution is insufficient to probe the small differences between the NA and the dip condition in terms of solute composition of the matrix and particles. In the peak condition, the Zn/Mg ratio of the particles is about 1.8 and the solutes in solid solution has significantly decreased.

An additional APT dataset from the peak condition is shown in the supplementary. This dataset indicated a microstructure with a homogeneous distribution of rod-shaped precipitates. In general, the peak aged condition of Al–Zn–Mg alloys is associated with a large number density of plate-like precipitates, such as η' and η_2, so that the dataset included in the supplementary is not regarded as representative for the microstructure, supported by the TEM observations. The composition of the particles in the additional dataset was similar to the one shown in Table 4, indicating that the precipitates in this condition are variants of η. As η_4 has a rod-like morphology and can be observed in the peak aged condition, often associated with defects, it is likely that most of the precipitates in the additional dataset are η_4 in a dislocation-rich region.

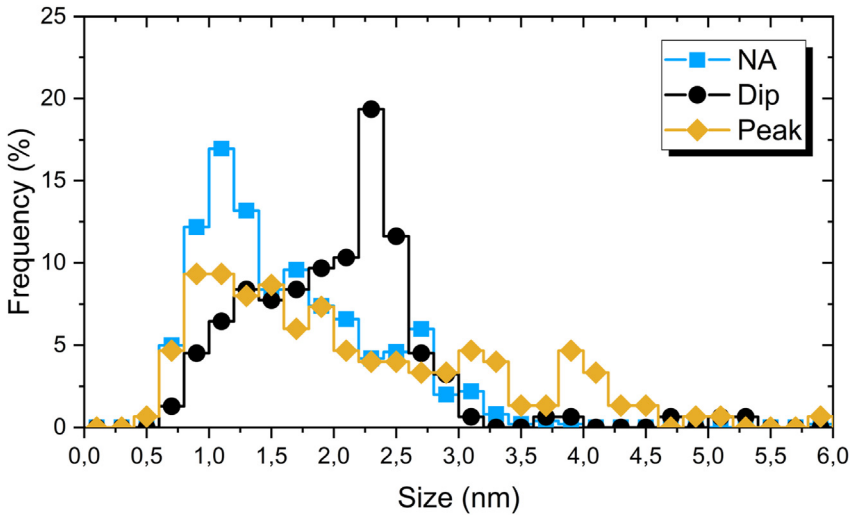

Fig. 4 – Particle size distribution for NA, dip and peak conditions measured by APT.

Table 4 – APT measurements of the bulk, matrix and particle composition in at.% in Mg and Zn and Mg + Zn for NA, dip and peak conditions, in addition to the Zn/Mg ratio of the particles.

		NA	Dip	Peak
Bulk	Mg	0.95 ± 0.02	0.93 ± 0.01	0.92 ± 0.01
	Zn	2.75 ± 0.02	2.54 ± 0.01	2.41 ± 0.01
	Mg + Zn	3.70 ± 0.03	3.47 ± 0.01	3.33 ± 0.01
Matrix	Mg	0.76 ± 0.02	0.79 ± 0.01	0.53 ± 0.01
	Zn	2.25 ± 0.02	2.14 ± 0.02	1.76 ± 0.03
	Mg + Zn	3.01 ± 0.03	2.93 ± 0.02	2.29 ± 0.03
Particles	Mg	5.84 ± 0.15	6.43 ± 0.15	9.66 ± 0.08
	Zn	11.69 ± 0.20	11.10 ± 0.20	17.06 ± 0.11
	Mg + Zn	17.53 ± 0.25	17.53 ± 0.25	26.72 ± 0.14
	Zn/Mg	2.00 ± 0.08	1.73 ± 0.07	1.76 ± 0.02

3.3. *Atomic structure evolution from NA to the peak aged condition*

Overview HAADF-STEM images from the three conditions are shown in Fig. 5. Images taken along the $\langle 001\rangle_{Al}$ and $\langle 110\rangle_{Al}$ zone axes are shown in Fig. 5a and b, respectively. A dense population of GPI zones in the form of connected TCOs is present in the NA condition, as seen in Fig. 5a. In addition to the GPI zones, a small population of fine precipitates with habit plane $\{111\}_{Al}$ was observed in Fig. 5b. As shown below, these precipitates can be categorised as η'. To assess the amount of η' and η_2 nucleated in each condition, at least 300 precipitates were investigated per condition. The projection of the disc-like η' and η_2 along an arbitrary $\langle 110\rangle_{Al}$ direction is either rod-like (viewed edge-on) or elliptical (viewed at 35° angle), the ratio between the precipitates viewed edge-on and face-on is one in this direction. Assuming that there are equal amounts of precipitates on each equivalent $\{111\}_{Al}$ plane, the number of $\eta' + \eta_2$, $N_{edge\text{-}on}$ seen edge-on in each condition was quantified. The occurrence of precipitates may be estimated as two times the occurrence of $N_{edge\text{-}on}$ ($2N_{edge\text{-}on}$), accounting for the uncounted elliptical precipitates [49]. The results are shown in Table 5. Only 2% of the precipitates in the NA condition were categorised as η', while all the others were assumed to be GPI zones or clusters. No GPII zones were observed in any of the conditions investigated.

At the dip condition, the structure of the clusters had clearly changed. In the $\langle 001\rangle_{Al}$ orientation, seen in Fig. 5c, very few connected TCOs were observed. Few of the precipitates exhibited ordering in this zone axis. In the $\langle 110\rangle_{Al}$ orientation (Fig. 5d), it was observed that more η' precipitates had nucleated during the 10 min of AA, and 17% of the precipitates was now categorised as η', c. f. Table 5. None of the other η precursors were observed in this condition.

At the peak condition, after AA for 5 h, the microstructure had coarsened significantly: Fig. 5f shows the presence of η', η_1 and seemingly spheroidal precipitates. 70% of the precipitates in the peak condition could be categorised as η' and η_2 precipitates, c. f. Table 5.

Fig. 6 shows images of higher magnification of the most prevalent precipitates observed in $\langle 001\rangle_{Al}$ and $\langle 110\rangle_{Al}$ zone axes as identified in the overview images in Fig. 5. Fig. 6a shows a typical GPI zone, comprising 5 TCOs connected along $\langle 411\rangle_{Al}$. Single TCOs were observed in both the dip and peak aged conditions, exemplified in Fig. 6b and c. These are most likely strings of TCOs stacked along the viewing direction. The center of the TCOs are indicated by the red circle, while the full TCOs are indicated by the yellow rectangles. A minor fraction of the observed clusters in the NA condition exhibited a structure similar to the ones in Fig. 6b–c.

The precipitates in Fig. 6d–f have the same width and are similar, but due to the different extension along the viewing direction, the intensities of the atomic columns appear different. This can lead to misinterpretation of the precipitate type. Note that all three precipitates have a width of $6d^{Al}_{111}$ and hence are identified as η' according to the categorising criteria given in the introduction.

3.4. *Precipitates in the peak aged condition*

Fig. 7 shows three different η precursors imaged in a $\langle 211\rangle_{Al}$ orientation with the same habit plane and orientation

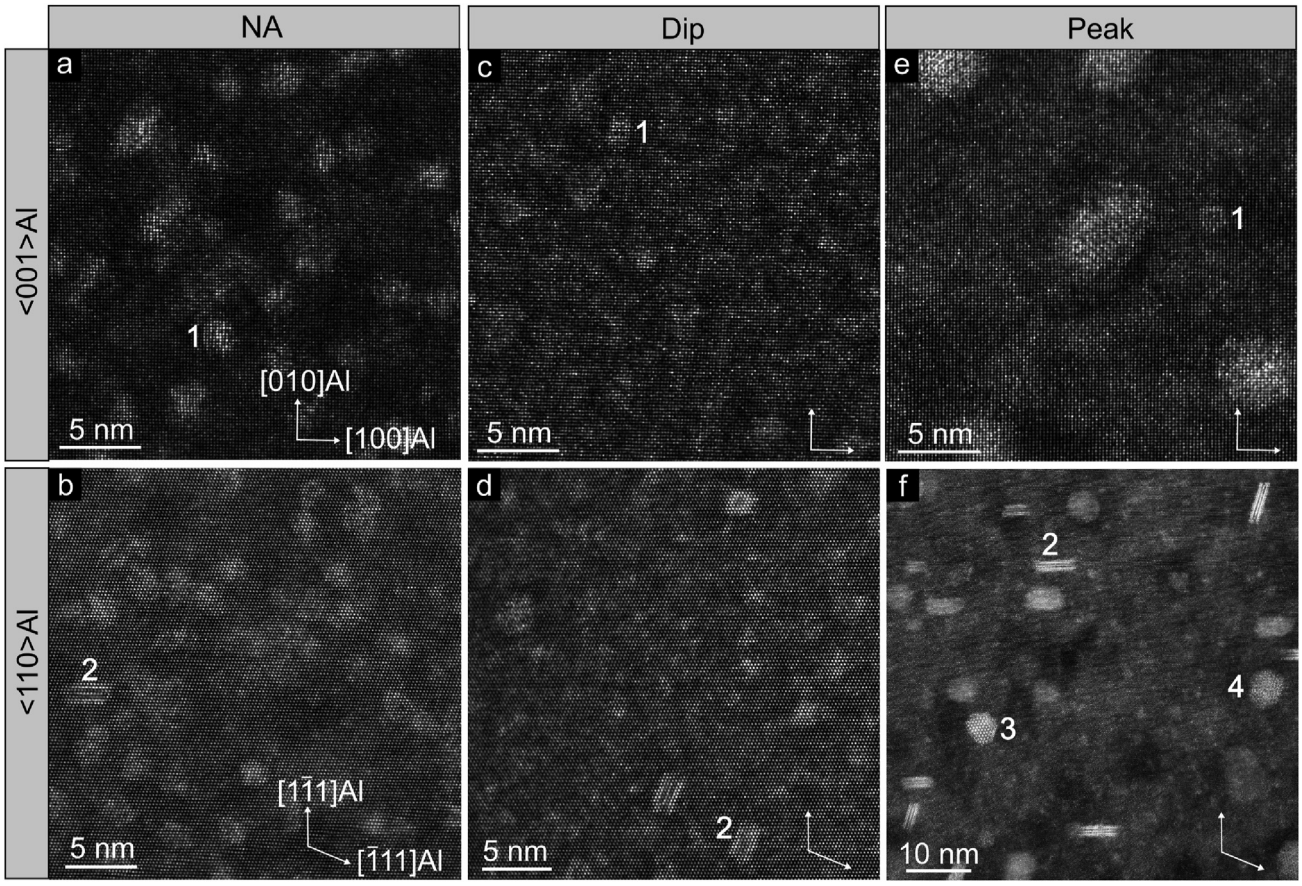

Fig. 5 – Overview HAADF-STEM images in $\langle 001\rangle_{Al}$ and $\langle 110\rangle_{Al}$ for 1 year NA (a, b), the dip (c, d) and the peak aged condition (e, f), respectively. The numbers indicate precipitates of interest: 1 - GPI zone, 2 - η', 3 - η_1 and 4 - spheroidal precipitate.

Table 5 – The relative occurrence of η' and η_2 precipitates compared to the total number of precipitates in the three conditions. In the NA and dip condition, the only η precursors observed were η', while in the peak aged condition, η', η_1 and η_2 were observed.

	NA	Dip	Peak
Occurrence of η precursors	2%	18%	70%

relationship. An example of an η' precipitate is shown in Fig. 7a. The rhomobohedral and orthorombic layers characteristic for η' are indicated by 'R' and 'O' in figure. InFig. 7b, a small η_2 particle is shown - the only η_2 precipitate found out of 20 precipitates in this orientation. The characteristic rhomobohedral and vertically mirrored rhomobohedral layers of η_2 are indicated by 'R' and 'R^{-1}' in Fig. 7b. The precipitate in Fig. 7c exhibits the same orientation relationship and habit plane as η' and η_2, but has a different atomic structure. This is highlighted in the figure, showing that such precipitates comprised both the 'O' layer of the η' and the 'R'/'R^{-1}' layer of η_2.

HAADF-STEM images of precipitates imaged along $\langle 110\rangle_{Al}$ in the peak condition are shown in Fig. 8a–c. Here, d-f show higher magnifications of the images in 8a-c, respectively. Fig. 8g–i are FFTs corresponding to 8a-c, respectively. The PED patterns (Fig. 8j-l) exhibit good correspondence with the respective FFTs in Fig. 8g–i. Fig. 8a shows an η_1 precipitate viewed along $[001]_\eta$. The projected unit cell is indicated in d. Both the FFT (Fig. 8g) and PED pattern (Fig. 8j) exhibit the characteristic hexagonal reflections of η when viewed along its principal, hexagonal axis.

Fig. 8b gives an example of η_1 viewed along $[100]_\eta$. The projected unit cell is indicated in the enlarged region in Fig. 8e. Here the characteristic R and R^{-1} layers are indicated. The corresponding FFT and PED pattern of η_1 in this projection are given in Fig. 8h and k, respectively, showing the two-fold symmetry of the crystal structure of the precipitate viewed along this projection.

In Fig. 8c, a precipitate with a crystal structure unrelated to the η' or η precipitates is shown. Its projected atomic structure is magnified in Fig. 8f. The FFT in Fig. 8i shows good correspondence with the PED pattern in Fig. 8l and exhibits a two-fold symmetry. The precipitate is identified as T′ since the PED pattern was found to correspond to FFTs or diffraction patterns of T′ presented in previous studies [45,50,51,73,74].

To quantify the precipitates in the peak condition, several large-area HAADF-STEM images, taken along $\langle 110\rangle_{Al}$, were analysed. An example is shown in Fig. 9. The precipitates were categorised as either η', η_1, η_2 or T′. Precipitates exhibiting a width of $6d^{Al}_{111}$ were categorised as η', thicker plates were categorised as η_2. This category necessarily includes faulted precipitates like to one imaged in Fig. 7c, since it is indistinguishable from η_2 in this projection. The results are shown in

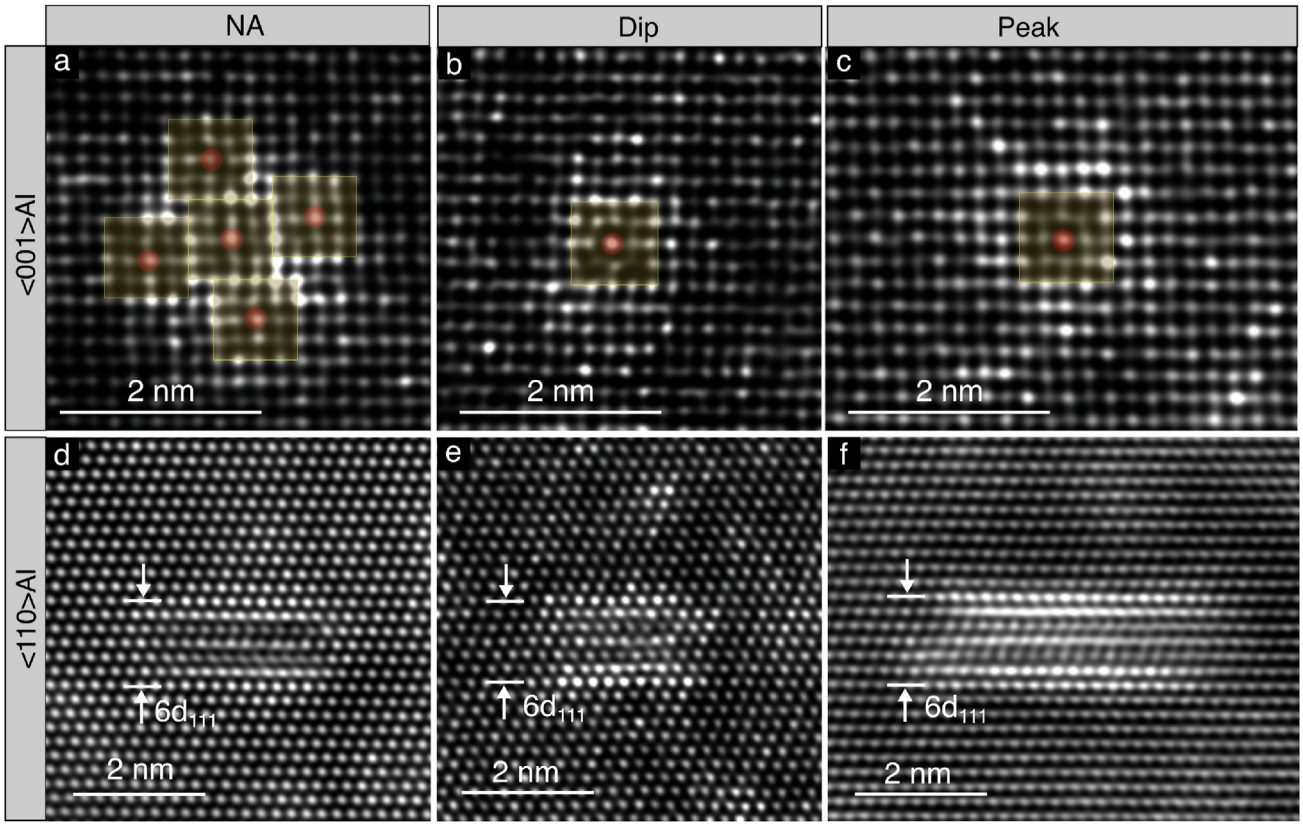

Fig. 6 – High magnification images of the precipitates in the three conditions. a: GPI zone comprised of five TCOs. b, c: Examples of single TCOs labeled '2′ and '3′ in Fig. 5b and c, respectively. The centers of the TCOs are indicated by the red circle, while the full TCOs are indicated by the yellow rectangles. d, e, f: η' precipitates in the NA, dip and peak condition, respectively.

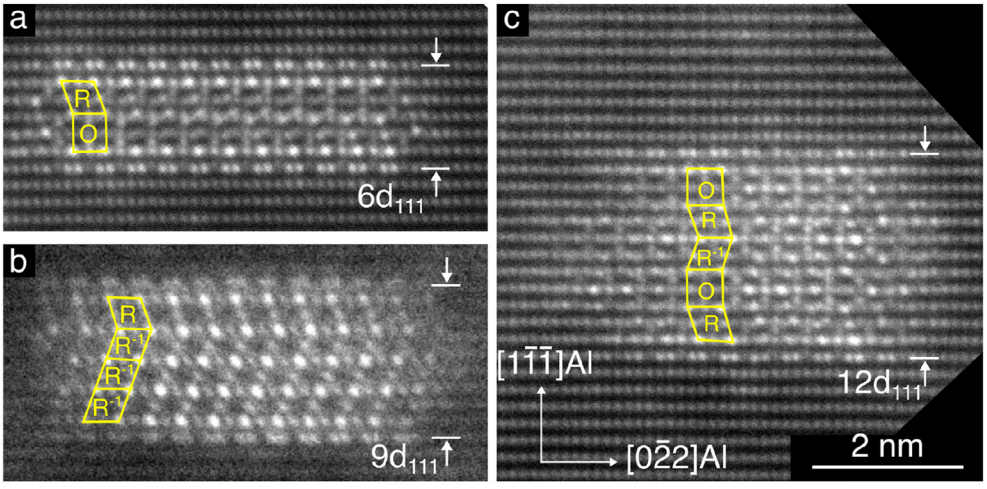

Fig. 7 – Smart-aligned HAADF-STEM images of precipitates with habit plane $\{111\}_{Al}$ viewed along ⟨211⟩ in the peak condition. a: η', b: η_2 and c: Faulted η precipitate with the same habit plane and orientation relationship as η' and η_2. The scale is the same for all three figures. Rhomobohedral, vertically mirrored rhomobohedral and orthorombic layers are indicated with R, R^{-1} and O, respectively.

Table 6 η' was the most prominent phase, followed by η_2. 6% of the precipitates were identified as the T′ phase, while 2% were found to be η_1. Note that the numbers in Table 6 only reflect identifiable precipitates, whereas the numbers in Table 5 considered all precipitates compared to the relative occurrence of η' and η_2.

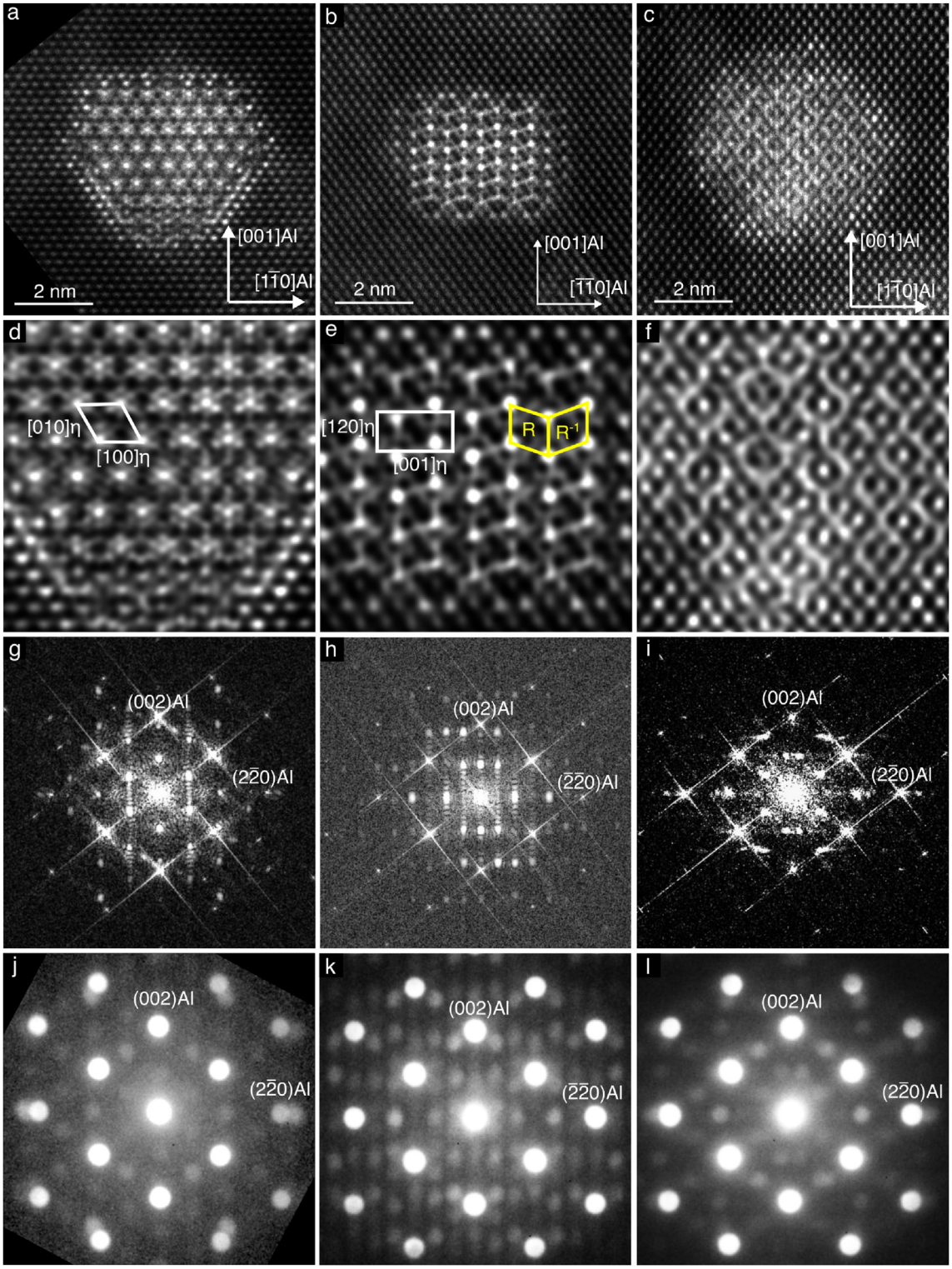

Fig. 8 – Precipitates in the peak condition viewed along $\langle 110 \rangle_{Al}$. a: η_1 precipitate viewed along $[001]_\eta$, b: η_1 viewed along $[100]_\eta$ and c: T′ phase. d, e and f: Enlarged, FFT filtered regions of the HAADF-STEM images in a, b and c, respectively. g, h and i: FFTs of a, b and c, respectively. j, k and l: PED patterns exhibiting a good correspondence with the FFTs in g, h and i, respectively. Rhomobohedral and vertically mirrored rhomobohedral layers are indicated with R and R^{-1}, respectively.

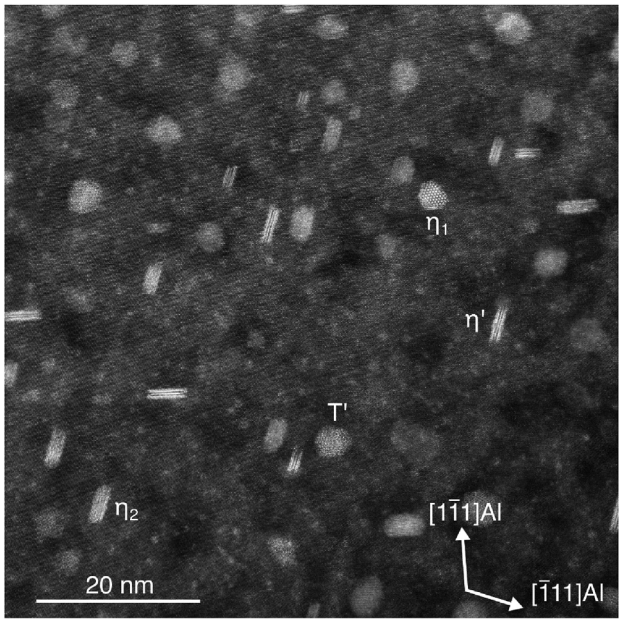

Fig. 9 – HAADF-STEM overview image of the precipitates in the peak aged condition. Examples of η', η_1, η_2 and T′ are indicated.

4. Discussion

The evolution of precipitates from the NA condition to peak aged condition was investigated by the means of hardness measurements, APT, atomically resolved HAADF-STEM and SPED. The one year NA condition contained a dense population of GPI zones. No GPII zones were observed, consistent with our previous works on other Al–Zn–Mg alloys in the same condition [4,19,63]. Interestingly, a small population of η' precipitates had already formed during NA. Based on the HAADF-STEM images, two percent of the precipitates in the NA condition could be identified as η'. In our experience, for a range of Al–Zn–Mg alloys, formation of developed η' at the low NA temperature seems to be common. To the authors' knowledge, this has not been reported before in these alloys. The co-existence of the GPI zones and η' precipitates during NA indicates that they form independently. This is supported by the work of Li et al. [28] who found a very early preference for the precipitates to exhibit a width of $6d^{Al}_{111}$ during AA at 120 °C.

The APT experiments revealed that the Zn/Mg ratio of the clusters in the NA condition was approximately 2. It is important to note that this average ratio incorporates both the GPI zones and the η' precipitates, since we were not able to separate the two morphologies with APT, due to the low aspect ratio of the η' precipitates in this condition. This is often not accounted for in the literature, since authors often assume the microstructure in the NA condition or early stages of low temperature AA to exclusively consist of GP zones and solute clusters [75–77]. This will affect the estimated Zn/Mg ratio of the GP zones in APT studies. The error is not large in the NA condition, due to the low occurrence of η' in such conditions. It might however introduce a larger error when estimating the Zn/Mg ratio of GPI zones during early stage AA. The occurrence of η' increases rapidly at elevated temperatures, as seen in the present study.

Table 6 – Quantification of the relative occurrence of the different precipitates observed in the peak condition.

	η'	η_1	η_2	T′
Counts (#)	124	4	54	12
Relative fraction	64%	2%	28%	6%

During the initial stages of AA at 140 °C, the hardness rapidly decreased. After AA for 10 min, i.e. the dip condition, the hardness reached a minimum of 88 HV. This is still significantly higher than the as-quenched hardness of 47 HV, indicating that the alloy undergoes a partial reversion, rather than a complete reversion. Hence, the formation of new η' precipitates overlaps with the dissolution of the GPI zones. This is in accordance with the results in the review article by Löffler et al. [2], who showed that Zn-rich Al–Zn–Mg alloys often undergo partial reversion. Interestingly, APT indicated that the clusters in the dip condition were larger compared to the clusters in the NA condition. The obstacle strength of the clusters in this condition is however lower as compared to the GPI zones in the NA condition, revealed by the hardness measurements. Based on HAADF-STEM imaging, the clusters in the dip condition showed less ordering as compared to the GPI zones in the NA condition. This indicates that the GPI zones are dissolving rapidly during the initial stages of AA.

HAADF-STEM showed that the η' precipitate occurrence increased from 2% in the NA condition to 18% in the dip condition, c. f. Table 5. Hence, the solutes released to the matrix from the dissolving GPI zones are consumed as the formation of new η' precipitates occurs in the early stages of AA. The η' precipitates in the dip condition were however less developed as compared to the η' precipitates observed in the peak aged condition.

The partial reversion of GPI zones is in literature often explained by the transformation of overcritical sized GPI zones into η' precipitates [2]. In our previous work on the atomic structure of GPI zones [18], we found no structural connection between the GPI zones and the η' precipitates. This indicates that the GPI zones cannot transform into η'. The present work also supports this, since no overcritical GPI zones were observed in the dip condition by TEM. If η' transformed from overcritical GPI zones, we would expect the dip condition to contain larger GPI zones than the NA condition, but this was not observed. Hence, we conclude that in this alloy, the partial reversion is realised by the dissolution of the GPI zones accompanied by the simultaneous formation of new η' precipitates. It is possible that the η' precipitates form preferentially from the solute traces of the GPI zones. The dissolution of the GPI zones may cause a high local supersaturation in the matrix, which is diminished by the formation of η' [2]. This is however challenging to prove or disprove experimentally.

The clusters exhibiting ordering in the dip condition appear to be single TCOs, which were also present at the peak aged condition, c. f. Fig. 6b and c. Whether these are traces

from the GPI zones in the NA condition or not is challenging to conclude. We do however note their presence, and that they are seemingly more thermally stable than the more developed GPI zones. Alternatively, the single TCOs may have nucleated after AA during room temperature storage between sample preparation and TEM observations. This is however not very likely. Since the dip condition was assumed to be an unstable condition, the samples were prepared directly before both the TEM and APT experiments, with a sample preparation time of about two-three hours.

At peak age, the microstructure coarsened significantly as compared to the NA and dip condition. This is evident from the 3D atom probe map in Fig. 3 of the peak condition. It is also reflected in the lower precipitate number density measured by APT, c. f. Table 3. HAADF-STEM imaging showed that the peak condition consisted of approximately 70% plate-like η' and η_2 precipitates. The η variants observed in this condition comprised η', η_1, η_2 and faulted η precipitates as the one in Fig. 7c. Liu et al. [34] described the faulted precipitates as precursors to the η_2 precipitates and named them η'_p. As mentioned in the introduction, there is disagreement in the literature regarding the terminology of precipitates in Al–Zn–Mg alloys, c. f. The precipitation sequences in Eqs. (2) and (3). By comparing images however, it becomes clear that the η' in Fig. 7a in the current work is similar to GP-η_p in Fig. 4b in Ref. [35]. The η_2 in Fig. 7b is similar to the η_p in Fig. 5d in Ref. [35]. Hence, the two precipitation sequences in Eq. (2) and Eq. (3) are equivalent. Therefore, we conclude that Liu et al. describe the η'_p precipitate as the transition phase between η' and η_2. This transition stage is most likely limited to a short period of time, thus proving this is challenging experimentally.

η' precipitates were identified as the main hardening phase in the peak aged condition, c. f. Table 6, while η_2 was the second most prominent phase. The average Zn/Mg ratio of all precipitates in the peak aged condition was approximately 1.8. As the Zn/Mg ratio of the η' is estimated to be around 1.4, this indicates that the other precipitates have a higher Zn/Mg ratio. For the η_1 and η_2 this is reasonable, since they have Zn/Mg ratios close to the equilibrium η-$MgZn_2$. It is also likely that the Zn/Mg ratio of η' varies with the alloy composition, as supported by calculations showing that the GPI zones are stable for a range of compositions [18].

T′ precipitates were also found in the peak condition. They appeared spheroidal, c. f. Fig. 8c. A majority of the T′ precipitates were found to be disordered, hence it was challenging to identify a projected unit cell. The FFT and PED patterns of the T′ phase viewed along $\langle 110 \rangle_{Al}$, however are characteristic and similar to the patterns presented in Refs. [45,50,51,73,74]. The crystal structure of T′ is assumed to be the similar to the equilibrium phase T-$Mg_{21}(Al, Zn)_{49}$ [42]. We note however, that the PED pattern of T′ along $\langle 110 \rangle_{Al}$ exhibits similarities with the diffraction pattern of the Z-phase in Al–Mg–Cu–Ag alloys, first presented by Chopra [78] and later by Mihara et al. [79]. The Z-phase is not isomorphous with the T phase. Comparing the atomic structure of the T′ phase with the Z-phase is part of ongoing work and will be published elsewhere. For the time being, we note the similarities and highlight that the crystal structure of T′ is not necessarily isostructural to the equilibrium T phase.

5. Conclusion

The evolution of precipitates in a 7003 alloy was studied by STEM, APT and hardness measurements. The alloy was naturally aged for one year before subjected to AA at 140 °C. The NA condition contained a dense population of GPI zones, co-existing with a small population of η' precipitates. The alloy experienced partial reversion of the GPI zones during the 10 first minutes by concurrent dissolution of GPI zones and formation of new η' precipitates. The occurrence of η' increased from 2% in the NA condition to 18% after 10 min of AA, with the consequence of a decreased average Zn/Mg ratio in the precipitates. The prevalence in the dip condition of single TCO clusters, rather than multiple connected TCO units comprising the GPI zones indicates that the GPI zones dissolve, rather than transform structurally to η'. No GPI zones were observed in the peak aged condition, hence 140 °C is above the dissolution temperature of this phase in the investigated alloy. The most prominent phase in the peak aged condition was η', followed by η_2. A small population of η_1 was also present. In addition, both APT and TEM indicated the presence of spheroidal precipitates, identified as the T′ phase. Based on STEM, approximately 30% of the precipitates were spheroidal, which may indicate a significant amount of T′ phases in these alloys.

Author contribution

E.T., S.S., C.D.M., S.W., B.H. and R.H. conceived, designed and supervised the research. E.T. conducted the (S)TEM experiments. S.S. conducted the hardness measurements and APT experiments. S.S. analysed the APT data with significant contribution from C.H. E.T. and S.S. prepared figures. E.T. and S.S. wrote the manuscript with input from all authors.

Data availability

The raw data used to reproduce the presented results are available in the Zenodo repository: https://doi.org/10.5281/zenodo.6655410.

Declaration of Competing Interest

The authors declare the following financial interests/personal relationships which may be considered as potential competing interests: Randi Holmestad reports financial support was provided by Research Council of Norway.

Acknowledgements

This work was supported by the NTNU Digital Transformation initiative 'Alldesign' (E.T. and R.H.) and The Research Council of Norway (NFR) through the project 'SumAl' (NFR: 294933) (C.D.M., S. W., R.H. & S.J.A., supported by Hydro, Benteler

Automotive Raufoss AS and Neuman Aluminium. The (S)TEM work was conducted on the NORTEM (NFR: 197405) infrastructure at the TEM Gemini Centre, Trondheim, Norway. The authors also wish to thank Hanne-Sofie Søreide for her support in the APT lab and Akash Gopal for conducting certain hardness measurements. NFR is acknowledged for funding the NTNU atom probe facility through the Norwegian Laboratory for Mineral and Materials Characterisation (MiMaC) project number: 269842.

Appendix A. Supplementary data

Supplementary data to this article can be found online at https://doi.org/10.1016/j.jmrt.2023.02.144.

REFERENCES

[1] Jensrud O. High strength aluminium alloys extrusions - a review of the thermo-mechanical-process in high performance profile manufacturing. Key Eng Mater 2011;491:11–8. https://doi.org/10.4028/WWW.SCIENTIFIC.NET/KEM.491.11. URL: https://www.scientific.net/KEM.491.11.

[2] Löffler H, Kovács I, Lendvai J. Decomposition processes in Al-Zn-Mg alloys. J Mater Sci 1983;18:2215–40. https://doi.org/10.1007/BF00541825. URL: https://link.springer.com/article/10.1007/BF00541825.

[3] Lendvai J. Precipitation and strengthening in aluminium alloys, in: aluminium alloys - ICAA5, vols. 217–222. Trans Tech Publications Ltd 1996:43–56. https://doi.org/10.4028/WWW.SCIENTIFIC.NET/MSF.217-222.43. URL: https://www.scientific.net/MSF.217-222.43.

[4] Lervik A, Marioara CD, Kadanik M, Walmsley JC, Milkereit B, Holmestad R. Precipitation in an extruded AA7003 aluminium alloy: observations of 6xxx-type hardening phases. Mater Des 2020;186:108204. https://doi.org/10.1016/J.MATDES.2019.108204.

[5] Dumitraschkewitz P, Gerstl SS, Stephenson LT, Uggowitzer PJ, Pogatscher S. Clustering in age-hardenable aluminum alloys. Adv Eng Mater 2018;20:1800255. https://doi.org/10.1002/ADEM.201800255. URL: https://onlinelibrary.wiley.com/doi/full/10.1002/adem.201800255 https://onlinelibrary.wiley.com/doi/abs/10.1002/adem.201800255 https://onlinelibrary.wiley.com/doi/10.1002/adem.201800255.

[6] Guinier A. Structure of age-hardened aluminium-copper alloys. 1938. https://doi.org/10.1038/142569b0. URL: https://www.nature.com/articles/142569b0.

[7] Preston G. LXXIV. The diffraction of X-rays by an age-hardening alloy of aluminium and copper. The structure of an intermediate phase. The London, Edinburgh, and Dublin Philosophical Magazine and Journal of Science 1938;26:855–71. https://doi.org/10.1080/14786443808562177. URL: https://www.tandfonline.com/doi/abs/10.1080/14786443808562177.

[8] Embury JD, Nicholson RB. The nucleation of precipitates: the system Al-Zn-Mg. Acta Metall 1965;13:403–17. https://doi.org/10.1016/0001-6160(65)90067-2.

[9] Schmalzried H, Gerold V. Röntgenographische Untersuchungen über die Aushärtung einer Aluminium-Magnesium-Zink-Legierung. Z Metallkd 1958;49:291–301. https://doi.org/10.1515/IJMR-1958-490603. URL: https://www.degruyter.com/document/doi/10.1515/ijmr-1958-490603/html.

[10] Thackery PA. The nature and morphology of precipitate in aluminium-zinc-magnesium alloys. J Inst Met 1968;96:228–35.

[11] Gjønnes J, Simensen CJ. An electron microscope investigation of the microstructure in an aluminium-zinc-magnesium alloy. Acta Metall 1970;18:881–90. https://doi.org/10.1016/0001-6160(70)90016-7.

[12] Degischer HP, Lacom W, Zahra A, Zahra CY. Decomposition processes in an Al-5% Zn-1% Mg alloy. Part II: electronmicroscopy investigations. Z Metallkd 1980;71:231–8. https://doi.org/10.1515/IJMR-1980-710405/MACHINEREADABLECITATION/RIS. URL: https://www.degruyter.com/document/doi/10.1515/ijmr-1980-710405/html.

[13] Chung T-F, Yang Y-L, Shiojiri M, Hsiao C-N, Li W-C, Tsao C-S, et al. An atomic scale structural investigation of nanometre-sized η precipitates in the 7050 aluminium alloy. Acta Mater 2019;174:351–68. https://doi.org/10.1016/J.ACTAMAT.2019.05.041.

[14] Bendo A, Matsuda K, Lervik A, Tsuru T, Nishimura K, Nunomura N, et al. An unreported precipitate orientation relationship in Al-Zn-Mg based alloys. Mater Char 2019;158:109958. https://doi.org/10.1016/J.MATCHAR.2019.109958.

[15] Marioara CD, Lefebvre W, Andersen SJ, Friis J. Atomic structure of hardening precipitates in an Al-Mg-Zn-Cu alloy determined by HAADF-STEM and first-principles calculations: relation to η-MgZn2. J Mater Sci 2013;48:3638–51. https://doi.org/10.1007/s10853-013-7158-3.

[16] Bendo A, Matsuda K, Lee S, Nishimura K, Nunomura N, Toda H, et al. Atomic scale HAADF-STEM study of η and η_1 phases in peak-aged Al–Zn–Mg alloys. J Mater Sci 2018;53:4598–611. https://doi.org/10.1007/s10853-017-1873-0. URL: https://link.springer.com/article/10.1007/s10853-017-1873-0.

[17] Berg LK, Gjønnes J, Hansen V, Li XZ, Knutson-Wedel M, Waterloo G, et al. GP-zones in Al-Zn-Mg alloys and their role in artificial aging. Acta Mater 2001;49:3443–51. https://doi.org/10.1016/S1359-6454(01)00251-8.

[18] Lervik A, Thronsen E, Friis J, Marioara CD, Wenner S, Bendo A, et al. Atomic structure of solute clusters in Al–Zn–Mg alloys. Acta Mater 2021;205:116574. https://doi.org/10.1016/j.actamat.2020.116574.

[19] Thronsen E, Frafjord J, Friis J, Marioara CD, Wenner S, Andersen SJ, et al. Studying GPI zones in Al-Zn-Mg alloys by 4D-STEM. Mater Char 2022;185:111675. https://doi.org/10.1016/J.MATCHAR.2021.111675.

[20] Hansen V, Karlsen OB, Langsrud Y, Gjønnes J. Precipitates, zones and transitions during aging of Al - Zn - Mg - Zr 7000 series alloy. Mater Sci Technol 2004;20:185–93. https://doi.org/10.1179/026708304225010424.

[21] Chemingui M, Khitouni M, Jozwiak K, Mesmacque G, Kolsi A. Characterization of the mechanical properties changes in an Al–Zn–Mg alloy after a two-step ageing treatment at 70° and 135 °C. Mater Des 2010;31:3134–9. https://doi.org/10.1016/J.MATDES.2009.12.033.

[22] Lorimer GW, Nicholson RB. Further results on the nucleation of precipitates in the Al-Zn-Mg system. Acta Metall 1966;14.

[23] Ryum N. Precipiation kinetics in an Al-Zn-Mg alloy. Z Metallkd 1975;66:338–43. https://doi.org/10.1515/IJMR-1975-660603/MACHINEREADABLECITATION/RIS. URL: https://www.degruyter.com/document/doi/10.1515/ijmr-1975-660603/html.

[24] Ferragut R, Somoza A, Dupasquier A. On the two-step ageing of a commercial Al - Zn - Mg alloy; a study by positron lifetime spectroscopy. J Phys Condens Matter 1996;8:8945. https://doi.org/10.1088/0953-8984/8/45/026. URL: https://

iopscience.iop.org/article/10.1088/0953-8984/8/45/026 https://iopscience.iop.org/article/10.1088/0953-8984/8/45/026/meta.
[25] Sha G, Cerezo A. Early-stage precipitation in Al-Zn-Mg-Cu alloy (7050). Acta Mater 2004;52:4503–16. https://doi.org/10.1016/j.actamat.2004.06.025.
[26] Lendvai J. The effect of vacancy-rich clusters on the decomposition processes in Al-Zn-Mg alloys. Cryst Res Technol 1984;19:1341–6. https://doi.org/10.1002/CRAT.2170191017. URL: https://onlinelibrary.wiley.com/doi/full/10.1002/crat.2170191017 https://onlinelibrary.wiley.com/doi/abs/10.1002/crat.2170191017 https://onlinelibrary.wiley.com/doi/10.1002/crat.2170191017.
[27] Momma K, Izumi F. VESTA 3 for three-dimensional visualization of crystal, volumetric and morphology data. J Appl Crystallogr 2011;44:1272–6. https://doi.org/10.1107/S0021889811038970. URL: http://scripts.iucr.org/cgi-bin/paper?db5098. https://journals.iucr.org/j/issues/2011/06/00/db5098/.
[28] Li YY, Kovarik L, Phillips PJ, Hsu YF, Wang WH, Mills MJ. High-resolution characterization of the precipitation behavior of an Al–Zn–Mg–Cu alloy. Phil Mag Lett 2012;92:166–78. https://doi.org/10.1080/09500839.2011.652682. URL: https://www.tandfonline.com/doi/abs/10.1080/09500839.2011.652682.
[29] Bendo A, Maeda T, Matsuda K, Lervik A, Holmestad R, Marioara CD, et al. Characterisation of structural similarities of precipitates in Mg–Zn and Al–Zn–Mg alloys systems. Phil Mag 2019;99:2619–35. https://doi.org/10.1080/14786435.2019.1637032. URL: https://www.tandfonline.com/doi/abs/10.1080/14786435.2019.1637032.
[30] Bendo A, Matsuda K, Nishimura K, Nunomura N, Tsuchiya T, Lee S, et al. The possible transition mechanism for the metastable phase in the 7xxx aluminium. Mater Sci Technol 2020;36:1621–7. https://doi.org/10.1080/02670836.2020.1821323. URL: https://www.tandfonline.com/doi/abs/10.1080/02670836.2020.1821323.
[31] Chung TF, Yang YL, Tai CL, Shiojiri M, Hsiao CN, Tsao CS, et al. HR-STEM investigation of atomic lattice defects in different types of η precipitates in creep-age forming Al–Zn–Mg–Cu aluminium alloy. Mater Sci Eng, A 2021;815:141213. https://doi.org/10.1016/J.MSEA.2021.141213.
[32] Chung TF, Yang YL, Huang BM, Shi Z, Lin J, Ohmura T, et al. Transmission electron microscopy investigation of separated nucleation and in-situ nucleation in AA7050 aluminium alloy. Acta Mater 2018;149:377–87. https://doi.org/10.1016/J.ACTAMAT.2018.02.045.
[33] Liu JZ, Chen JH, Yang XB, Ren S, Wu CL, Xu HY, et al. Revisiting the precipitation sequence in Al-Zn-Mg-based alloys by high-resolution transmission electron microscopy. Scripta Mater 2010;63:1061–4. https://doi.org/10.1016/j.scriptamat.2010.08.001.
[34] Liu JZ, Chen JH, Yuan DW, Wu CL, Zhu J, Cheng ZY. Fine precipitation scenarios of AlZnMg(Cu) alloys revealed by advanced atomic-resolution electron microscopy study Part I: structure determination of the precipitates in AlZnMg(Cu) alloys. Mater Char 2015;99:277–86. https://doi.org/10.1016/J.MATCHAR.2014.11.028.
[35] Liu JZ, Chen JH, Liu ZR, Wu CL. Fine precipitation scenarios of AlZnMg(Cu) alloys revealed by advanced atomic-resolution electron microscopy study Part II: fine precipitation scenarios in AlZnMg(Cu) alloys. Mater Char 2015;99:142–9. https://doi.org/10.1016/J.MATCHAR.2014.11.027.
[36] Cao F, Zheng J, Jiang Y, Chen B, Wang Y, Hu T. Experimental and DFT characterization of η nano-phase and its interfaces in AlZnMgCu alloys. Acta Mater 2019;164:207–19. https://doi.org/10.1016/J.ACTAMAT.2018.10.045.
[37] Andersen SJ, Marioara CD, Friis J, Wenner S, Holmestad R. Precipitates in aluminium alloys. Adv Phys X 2018;3:790–814. https://doi.org/10.1080/23746149.2018.1479984. URL: https://www.tandfonline.com/doi/abs/10.1080/23746149.2018.1479984.
[38] Li XZ, Hansen V, Gjønnes J, Wallenberg LR. HREM study and structure modeling of the η phase, the hardening precipitates in commercial Al–Zn–Mg alloys. Acta Mater 1999;47:2651–9. https://doi.org/10.1016/S1359-6454(99)00138-X.
[39] Bergman G, Waugh J, Pauling L. The crystal structure of the metallic phase Mg32(Al, Zn)49. Acta Crystallogr 1957;10:254–9. URL: //scripts.iucr.org/cgi-bin/paper?a01974. doi:10.1107/S0365110X57000808.
[40] Auld JH, Causland SM. The metastable T phase in Al-Zn-Mg and Al-Ag-Mg alloys. Met Sci 1976;10.
[41] Sun W, Lincoln FJ, Sugiyama K, Hiraga K. Structure refinement of (Al, Zn)49Mg32-type phases by single-crystal X-ray diffraction. Mater Sci Eng, A 2000;294–296:327–30. https://doi.org/10.1016/S0921-5093(00)01094-7.
[42] Bigot A, Auger P, Chambreland S, Blavette D, Reeves A. Atomic scale imaging and analysis of T' precipitates in Al-Mg-Zn alloys. Microsc Microanal Microst 1997;8:103–13. https://doi.org/10.1051/mmm:1997109. URL:.
[43] Hou S, Liu P, Zhang D, Zhang J, Zhuang L. Precipitation hardening behavior and microstructure evolution of Al–5.1 Mg–0.15Cu alloy with 3.0Zn (wt%) addition. J Mater Sci 2018;53:3846–61. https://doi.org/10.1007/s10853-017-1811-1. URL: https://link.springer.com/article/10.1007/s10853-017-1811-1.
[44] Hou S, Zhang D, Ding Q, Zhang J, Zhuang L. Solute clustering and precipitation of Al-5.1Mg-0.15Cu-xZn alloy. Mater Sci Eng, A 2019;759:465–78. https://doi.org/10.1016/J.MSEA.2019.05.066.
[45] Tang HP, Wang QD, Luo C, Lei C, Liu TW, Li ZY, et al. Effects of aging treatment on the precipitation behaviors and mechanical properties of Al-5.0Mg-3.0Zn-1.0Cu cast alloys. J Alloys Compd 2020;842:155707. https://doi.org/10.1016/J.JALLCOM.2020.155707.
[46] Stemper L, Tunes MA, Dumitraschkewitz P, Mendez-Martin F, Tosone R, Marchand D, et al. Giant hardening response in AlMgZn(Cu) alloys. Acta Mater 2021;206:116617. https://doi.org/10.1016/J.ACTAMAT.2020.116617.
[47] Guo C, Zhang H, Wu Z, Shen X, Wang P, Li B, et al. An atomic-resolution investigation of precipitation evolution in Al-Mg-Ag alloys. Mater Lett 2019;248:231–5. https://doi.org/10.1016/J.MATLET.2019.04.054.
[48] Cao C, Zhang D, Zhuang L, Zhang J. Improved age-hardening response and altered precipitation behavior of Al-5.2Mg-0.45Cu-2.0Zn (wt%) alloy with pre-aging treatment. J Alloys Compd 2017;691:40–3. https://doi.org/10.1016/J.JALLCOM.2016.08.206.
[49] Zou Y, Wu X, Tang S, Zhu Q, Song H, Cao L. Co-precipitation of T and η phase in Al-Zn-Mg-Cu alloys. Mater Char 2020;169:110610. https://doi.org/10.1016/J.MATCHAR.2020.110610.
[50] Zou Y, Wu X, Tang S, Zhu Q, Song H, Guo M, et al. Correlation between bulk and precipitate composition in Al-Zn-Mg-Cu alloys. Phil Mag Lett 2022;102:41–52. https://doi.org/10.1080/09500839.2021.1998690. URL: https://www.tandfonline.com/doi/abs/10.1080/09500839.2021.1998690.
[51] Zou Y, Wu X, Tang S, Zhu Q, Song H, Guo M, et al. Investigation on microstructure and mechanical properties of Al-Zn-Mg-Cu alloys with various Zn/Mg ratios. J Mater Sci Technol 2021;85:106–17. https://doi.org/10.1016/J.JMST.2020.12.045.
[52] Kelly TF, Miller MK. Atom probe tomography. Rev Sci Instrum 2007;78:031101. https://doi.org/10.1063/1.2709758. URL: https://aip.scitation.org/doi/abs/10.1063/1.2709758.

[53] Danoix F, Miller MK, Bigot A. Analysis conditions of an industrial Al–Mg–Si alloy by conventional and 3D atom probes. Ultramicroscopy 2001;89:177–88. https://doi.org/10.1016/S0304-3991(01)00098-5.
[54] Famelton JR, Hughes GM, Williams CA, Barbatti C, Moody MP, Bagot PA. Xenon plasma focussed ion beam preparation of an Al-6XXX alloy sample for atom probe tomography including analysis of an α-Al(Fe,Mn)Si dispersoid. Mater Char 2021;178:111194. https://doi.org/10.1016/J.MATCHAR.2021.111194.
[55] Wenner S, Lervik A, Thronsen E, Marioara CD, Kubowicz S, Holmestad R. Copper enrichment on aluminium surfaces after electropolishing and its effect on electron imaging and diffraction. Mater Char 2021;172:110846. https://doi.org/10.1016/J.MATCHAR.2020.110846.
[56] Hatzoglou C. Napa. 2022. URL: https://www.ntnu.edu/ima/research/apt.
[57] Karnesky RA, Sudbrack CK, Seidman DN. Best-fit ellipsoids of atom-probe tomographic data to study coalescence of γ (L12) precipitates in Ni–Al–Cr. Scripta Mater 2007;57:353–6. https://doi.org/10.1016/J.SCRIPTAMAT.2007.04.020.
[58] Gault B, Moody MP, De Geuser F, Tsafnat G, La Fontaine A, Stephenson LT, et al. Advances in the calibration of atom probe tomographic reconstruction. J Appl Phys 2009;105:034913. https://doi.org/10.1063/1.3068197. URL: https://aip.scitation.org/doi/abs/10.1063/1.3068197.
[59] Lefebvre W, Vurpillot F, Sauvage X, editors. Atom probe tomography; 2016.
[60] Hyde JM, Dacosta G, Hatzoglou C, Weekes H, Radiguet B, Styman PD, et al. Analysis of radiation damage in light water reactors: comparison of cluster analysis methods for the analysis of atom probe data. Microsc Microanal 2017;23:366–75. https://doi.org/10.1017/S1431927616012678. URL: https://www.cambridge.org/core/journals/microscopy-and-microanalysis/article/analysis-of-radiation-damage-in-light-water-reactors-comparison-of-cluster-analysis-methods-for-the-analysis-of-atom-probe-data/6DC1831A50B0DEC9EED3EF4CC86B7CD0.
[61] Vurpillot F, Bostel A, Blavette D. Trajectory overlaps and local magnification in three-dimensional atom probe. Appl Phys Lett 2000;76:3127. https://doi.org/10.1063/1.126545. URL: https://aip.scitation.org/doi/abs/10.1063/1.126545.
[62] Miller MK, Hetherington MG. Local magnification effects in the atom probe. Surf Sci 1991;246:442–9. https://doi.org/10.1016/0039-6028(91)90449-3.
[63] Shah S, Thronsen E, Hatzoglou C, Wenner S, Marioara CD, Holmestad R, et al. Effect of cyclic ageing on the early-stage clustering in Al–Zn–Mg(-Cu) alloys. Mater Sci Eng, A 2022;846:143280. https://doi.org/10.1016/J.MSEA.2022.143280. URL: https://linkinghub.elsevier.com/retrieve/pii/S0921509322006803.
[64] Lawitzki R, Stender P, Schmitz G. Compensating local magnifications in atom probe tomography for accurate analysis of nano-sized precipitates. Microsc Microanal 2021;27:499–510. https://doi.org/10.1017/S1431927621000180. URL: https://www.cambridge.org/core/journals/microscopy-and-microanalysis/article/compensating-local-magnifications-in-atom-probe-tomography-for-accurate-analysis-of-nanosized-precipitates/5DC19F187E0422EC6BC705AD245D9379.
[65] Vurpillot F, Oberdorfer C. Modeling atom probe tomography: a review. Ultramicroscopy 2015;159:202–16. https://doi.org/10.1016/J.ULTRAMIC.2014.12.013.
[66] Marceau RK, Stephenson LT, Hutchinson CR, Ringer SP. Quantitative atom probe analysis of nanostructure containing clusters and precipitates with multiple length scales. Ultramicroscopy 2011;111:738–42. https://doi.org/10.1016/J.ULTRAMIC.2010.12.029.
[67] Jenkins BM, London AJ, Riddle N, Hyde JM, Bagot PA, Moody MP. Using alpha hulls to automatically and reproducibly detect edge clusters in atom probe tomography datasets. Mater Char 2020;160:110078. https://doi.org/10.1016/J.MATCHAR.2019.110078.
[68] Jones L, Yang H, Pennycook TJ, Marshall MS, Van Aert S, Browning ND, et al. Smart Align—a new tool for robust non-rigid registration of scanning microscope data. Advanced Structural and Chemical Imaging 2015;1:1–16. https://doi.org/10.1186/s40679-015-0008-4. URL: https://link.springer.com/article/10.1186/s40679-015-0008-4.
[69] Barnard JS, Johnstone DN, Midgley PA. High-resolution scanning precession electron diffraction: alignment and spatial resolution. Ultramicroscopy 2017;174:79–88. https://doi.org/10.1016/j.ultramic.2016.12.018.
[70] Mir JA, Clough R, MacInnes R, Gough C, Plackett R, Shipsey I, et al. Characterisation of the Medipix3 detector for 60 and 80 keV electrons. Ultramicroscopy 2017;182:44–53. https://doi.org/10.1016/j.ultramic.2017.06.010.
[71] Johnstone DN, Crout P, Nord M, Laulainen J, Høgås S, Opheim E, et al. pyxem/pyxem: pyxem 0.13.3. 2021. https://doi.org/10.5281/ZENODO.5075520. URL: https://zenodo.org/record/5075520.
[72] De Geuser F, Lefebvre W. Determination of matrix composition based on solute-solute nearest-neighbor distances in atom probe tomography. Microsc Res Tech 2011;74:257–63. https://doi.org/10.1002/jemt.20899. URL: https://analyticalsciencejournals.onlinelibrary.wiley.com/doi/10.1002/jemt.20899.
[73] Bernole M, Graf R. Influence du zinc sur la décomposition de la solution solide sursaturée Al-Mg. Mem Sci Rev Metall 1972;69:123–9.
[74] Takata N, Ishihara M, Suzuki A, Kobashi M. Microstructure and strength of a novel heat-resistant aluminum alloy strengthened by T-Al6Mg11Zn11 phase at elevated temperatures. Mater Sci Eng, A 2019;739:62–70. https://doi.org/10.1016/J.MSEA.2018.10.034.
[75] Ortner SR, Grovenor CR, Shollock BA. On the structure and composition of G-P zones in high purity AlZnMg alloys. Scripta Metall 1988;22:839–42. https://doi.org/10.1016/S0036-9748(88)80060-7.
[76] Wang YL, Song YY, Jiang HC, Li ZM, Zhang D, Rong LJ. Variation of nanoparticle fraction and compositions in two-stage double peaks aging precipitation of AlZnMg alloy. Nanoscale Res Lett 2018;13:1–7. https://doi.org/10.1186/s11671-018-2542-1. URL: https://nanoscalereslett.springeropen.com/articles/10.1186/s11671-018-2542-1.
[77] Lee SH, Jung JG, Baik SI, Seidman DN, Kim MS, Lee YK, et al. Precipitation strengthening in naturally aged Al–Zn–Mg–Cu alloy. Mater Sci Eng, A 2021;803:140719. https://doi.org/10.1016/J.MSEA.2020.140719.
[78] Deep Chopra H, Muddle BC, Polmear IJ. The structure of primary strengthening precipitates in an Al-1.5wt% Cu-4.0wt % Mg-0.5wt% Ag alloy. Philosophy 1996;73:351–8. https://doi.org/10.1080/095008396180623. URL: https://www.tandfonline.com/doi/abs/10.1080/095008396180623.
[79] Mihara M, Marioara CD, Andersen SJ, Holmestad R, Kobayashi E, Sato T. Precipitation in an Al–Mg–Cu alloy and the effect of a low amount of Ag. Mater Sci Eng, A 2016;658:91–8. https://doi.org/10.1016/J.MSEA.2016.01.087.